

# Three-dimensional sphericity, roundness and fractal dimension of sand particles

B. ZHOU\*, J. WANG† and H. WANG\*

Particle morphological features at different scale levels hold the key to understanding the geological origin and mechanical behaviour of natural sands. In this context, it is necessary to characterise and quantify these morphological features by defining a series of reasonable descriptors. In this study, based on X-ray micro-computed tomographic ( $\mu$ CT) images collected from a series of image-processing techniques, the authors first introduced spherical harmonic analysis to reconstruct a three-dimensional (3D) realistic surface of the sand particles. Then 3D sphericity, roundness and fractal dimension were introduced to define the global form, local features and surface textures of the particle morphology. Based on the spherical harmonic-reconstructed surface, a novel framework was established to measure the descriptors of 3D sphericity, roundness and fractal dimension of sand particles. The 3D fractal dimension was an original descriptor used to characterise the fractal nature of the surface textures of real sand particle morphology. By using the proposed methods, these morphological descriptors were measured for two types of natural sand particle. The statistical results show clear correlations between different descriptors at different characteristic scales. The correlation relies heavily upon the distance between the characteristic scales of the morphological descriptors.

**KEYWORDS:** discrete-element modelling; fractals; sands; soil classification

## INTRODUCTION

Particle morphology is an inherent soil characteristic that plays an important role in understanding the mechanical behaviour of natural sands. Many experimental studies have shown that the macroscopic mechanical properties of sands, such as their compressibility, shear strength, crushability and critical state behaviour, are highly influenced by the morphological features of the particles (Guo & Su, 2007; Rousé *et al.*, 2008; Tsomokos & Georgiannou, 2010; Altuhafi & Coop, 2011). As an alternative to investigating fundamental soil behaviour, the discrete-element method, first proposed by Cundall & Strack (1979), has made significant contributions to the elucidation of the micromechanics of particle morphology that affect the mechanical properties of sands (Wang & Gutierrez, 2010; Mahmood & Iwashita, 2011; Zhou *et al.*, 2013). To determine the effects of particle morphology on mechanical properties of sands in both experimental and numerical frameworks, it is necessary to characterise and quantify the morphological features of the particle in advance. In this context, three descriptors, including sphericity, roundness and fractal dimension, are widely accepted to define particle morphology at different length scales in terms of global form, local features and surface textures (Soga & Mitchell, 2005; Blott & Pye, 2008). The fractal dimension, which characterises the self-similar nature of particle morphology, is a scientific topic that has intrigued many authors (e.g. Hyslip & Vallejo, 1997; Santamarina & Cho, 2004; Langroudi *et al.*, 2014; Hanaor *et al.*, 2016).

Sphericity and roundness have traditionally been used to classify and quantify the morphological properties of soils in engineering and geology (Mehring & McBride, 2007; Santamarina & Cho, 2014). According to Wadell (1935), sphericity is quantified by comparing the surface area of a particle to that of a sphere with equal volume, and roundness is quantified by the average ratio of the curvature radius of all corners to the radius of the largest inscribed sphere of a particle. In engineering applications, two-dimensional (2D) sphericity and roundness are easily measured by comparing the microscopic view with the standard chart provided by Krumbein & Sloss (1963) and ASTM International (ASTM, 2009). With the development of micrography and image-processing techniques, 2D sphericity, roundness and some other descriptors (e.g. compactness, convexity, angularity and principal dimensions) can be measured by image analysis and computational geometry from 2D projections of particles (Mora & Kwan, 2000; Sukumaran & Ashmawy, 2001; Altuhafi *et al.*, 2012). To quantify the surface textures and roughness details of particles, different definitions have been introduced, including the Alshibli *et al.* (2014) material roughness indices (i.e. average and root-mean-square roughness) for a local area, Zheng & Hryciw (2015) statistical indices (i.e. locally weighted regression and  $k$ -fold cross-validation) and the Fourier descriptors of Bowman *et al.* (2001) and Mollon & Zhao (2012) for 2D projections.

With regard to the earlier studies in a 2D framework, it should be emphasised that measuring 2D sphericity, roundness and fractal dimension from a random projection of particles always results in random and inaccurate values. Hence, the measurement of three-dimensional (3D) sphericity, roundness and fractal dimension is significant for the authenticity and accuracy of the quantification of particle morphology. In the past two decades, the development of X-ray micro-computed tomography ( $\mu$ CT) technology has provided a powerful tool for 3D visualisation and characterisation of the internal microstructures and morphological features of sand particles (Fonseca *et al.*, 2012; Alshibli

Manuscript received 8 August 2016; revised manuscript accepted 11 April 2017.

Discussion on this paper is welcomed by the editor.

\* Department of Civil Engineering and Mechanics, Huazhong University of Science and Technology, Wuhan, P. R. China.

† Department of Architecture and Civil Engineering, City University of Hong Kong, Kowloon, Hong Kong.

*et al.*, 2014; Zhao *et al.*, 2015). Based on  $\mu$ CT images, the calculation methods of these 3D morphological factors can be divided into two groups. The first relies on the application of image analysis and computational geometry to the  $\mu$ CT images. It is easy to measure the volume, the moment of inertia and the principal dimensions of the particles by applying simple algorithms to their component voxels (Fonseca *et al.*, 2012; Zhao *et al.*, 2015). However, it is still a challenge to measure the reasonable particle surface area due to its scale-dependent characteristic (Hanaor *et al.*, 2014) and the error in boundary-detection algorithms (Fonseca, 2011). From  $\mu$ CT images, a particle's surface can be captured by a series of boundary voxels that are identified by the boundary-detection algorithm and connectivity criterion. However, the voxel-constructed surface is always characterised by a saw-tooth pattern and overlapping voxels induced by the high-order connectivity. For this reason, at the analysis scale of  $\mu$ CT resolution, the voxel-constructed surface always results in an overestimation of the reasonable surface area that greatly influences the accuracy of the measured sphericity (Zhou *et al.*, 2015). Moreover, it is also impossible to obtain the correct surface curvature and roundness of the particle from this kind of unsmooth surface.

The other group mainly includes mathematical approaches to calculating the geometric properties based on a particle surface reconstructed from  $\mu$ CT images (Alshibli *et al.*, 2014; Zhao & Wang, 2016). To reconstruct the particle surface, a variety of smoothing algorithms (Field, 1988; Kobbelt *et al.*, 2001) have been proposed to simultaneously remove the stair-steps and preserve the overall particle morphology. In this context, the efficiency of surface smoothing relies heavily upon the  $\mu$ CT resolution and the algorithm mechanism. Mathematically, particle surfaces reconstructed in this fashion are still not strictly continuous and differentiable, which leads to an inaccurate estimate of the surface curvature and roundness. To overcome this problem, Mollon & Zhao (2013, 2014) and Hanaor *et al.* (2015) proposed the production of virtual sand particles through the 3D interpolation of three orthogonal 2D cross-sections simulated by Fourier descriptors and fractal geometry. However, the artificial choice of these cross-sections probably resulted in a loss of the local features of the particle morphology, especially for highly irregular particles. For these reasons, the authors introduced a more sophisticated method using spherical harmonic (SH) analysis to characterise the 3D particle morphology and reconstruct its continuous particle surface (Zhou & Wang, 2015, 2017; Zhou *et al.*, 2015). In addition, the measurement of 3D fractal dimension for the closed surfaces of sand particles is still a major challenge that has not yet been overcome.

Hence, this study mainly developed practical approaches to calculate the 3D sphericity and roundness of real sand particles and further proposed a novel method to calculate the fractal dimension for a 3D closed particle surface. First, high-resolution X-ray scanning was conducted to obtain  $\mu$ CT images of two types of natural sand particles: Leighton Buzzard sand (LBS) particles and highly decomposed granite (HDG) particles. A series of image-processing techniques were then applied to the  $\mu$ CT images to extract the morphological information of each individual particle. The 3D particle surface was then reconstructed using SH analysis. Based on the SH-reconstructed particle surface, calculations of the surface area and local surface curvature were developed and discussed to further measure the 3D sphericity and roundness of the sand particles. Furthermore, a fractal dimension for the 3D closed surface of sand particles was defined, and its innovative measurement method was established by combining SH analysis and image analysis.

The statistics of these morphological descriptors are discussed here to validate the efficiency of the proposed calculation methods in this study.

## RECONSTRUCTION OF PARTICLE SURFACE

### *$\mu$ CT reconstruction and image processing*

Leighton Buzzard sand is quarried near the town of Leighton Buzzard in southeast England. It comes from the lower Greensand sequence, which was deposited in shallow sea and estuarine environments. The mineralogy is predominantly quartz with some feldspar and is characterised by chemical inertness and considerable hardness. The rounded and smooth particle morphology, as shown in Figs 1(a) and 1(c), may be the result of geological transportation processes. HDG, commonly found in Hong Kong, is mainly produced from the weathering and erosion of granitic rock outcrops. The particle morphology of HDG is always characterised by local angularity, roughness and some surface cavities, as shown in Figs 1(b) and 1(d). To implement the  $\mu$ CT scanning of the sand particles, about 120 LBS particles and 80 HDG particles between 1.18 mm and 2.36 mm were randomly selected from the screening packing. For each type of sand, several layers of particles were placed in a small polycarbonate pipe with a diameter of 16 mm and a height of 20 mm and fixed with silicone oil, as illustrated in Figs 1(a) and 1(b). A Carl Zeiss CT system (Metrotom 1500), provided by the Shenzhen Meixin Testing Technology Co. Ltd was used to conduct high-resolution X-ray  $\mu$ CT scanning and volume reconstruction of these two specimens. The voxel size of the reconstructed  $\mu$ CT images was 32.65  $\mu$ m due to the size of the specimen and the total pixels of the detector.

To extract and separate the scanned particles, the reconstructed 3D  $\mu$ CT images were put through a series of image-processing steps. The built-in 3D segmentation plug-in (Ollion *et al.*, 2013) within the image-processing package ImageJ (Abramoff *et al.*, 2004) was used in this study. These image-processing techniques mainly included segmenting different phases, reducing noise and separating and labelling individual particles. The solid phases (i.e. sand particles) were first distinguished from the void and silicone grease using thresholding, and binary CT images were obtained, with the solid pixels being white and the background pixels black. A 3D median filter with an intensity level of five pixels was then used to reduce the noise within the binary  $\mu$ CT images. To separate the particles in contact, a modified 3D watershed was applied to the  $\mu$ CT images to prevent over-segmentation. Finally, the individual particles were labelled with sequential grey levels using a simple segmentation algorithm. The processed  $\mu$ CT images were rendered and visualised in Figs 1(c) and 1(d).

### *Spherical harmonic reconstruction of particle surface*

The authors proposed to reconstruct the particle surface by SH analysis, which has been proven to be a powerful tool to represent particle morphological features at multiple scale levels (Zhou & Wang, 2015, 2017; Zhou *et al.*, 2015). For completeness, the SH theory used is briefly introduced here. Within the  $\mu$ CT images that were subjected to the image-processing techniques mentioned in the previous section, the voxels of each particle could be easily identified by their labelled grey level. The intrinsic function 'bwperim' in Matlab (Mathworks, 2010) was then used to detect the boundary voxels of a selected particle. A set of marginal vertices ( $x$ ,  $y$ ,  $z$ ) can be determined by the spatial positions of these boundary voxels and by the voxel resolution (i.e. the width of each voxel). As expressed in equation (1), the first step of SH analysis is to expand the polar radius from a unit

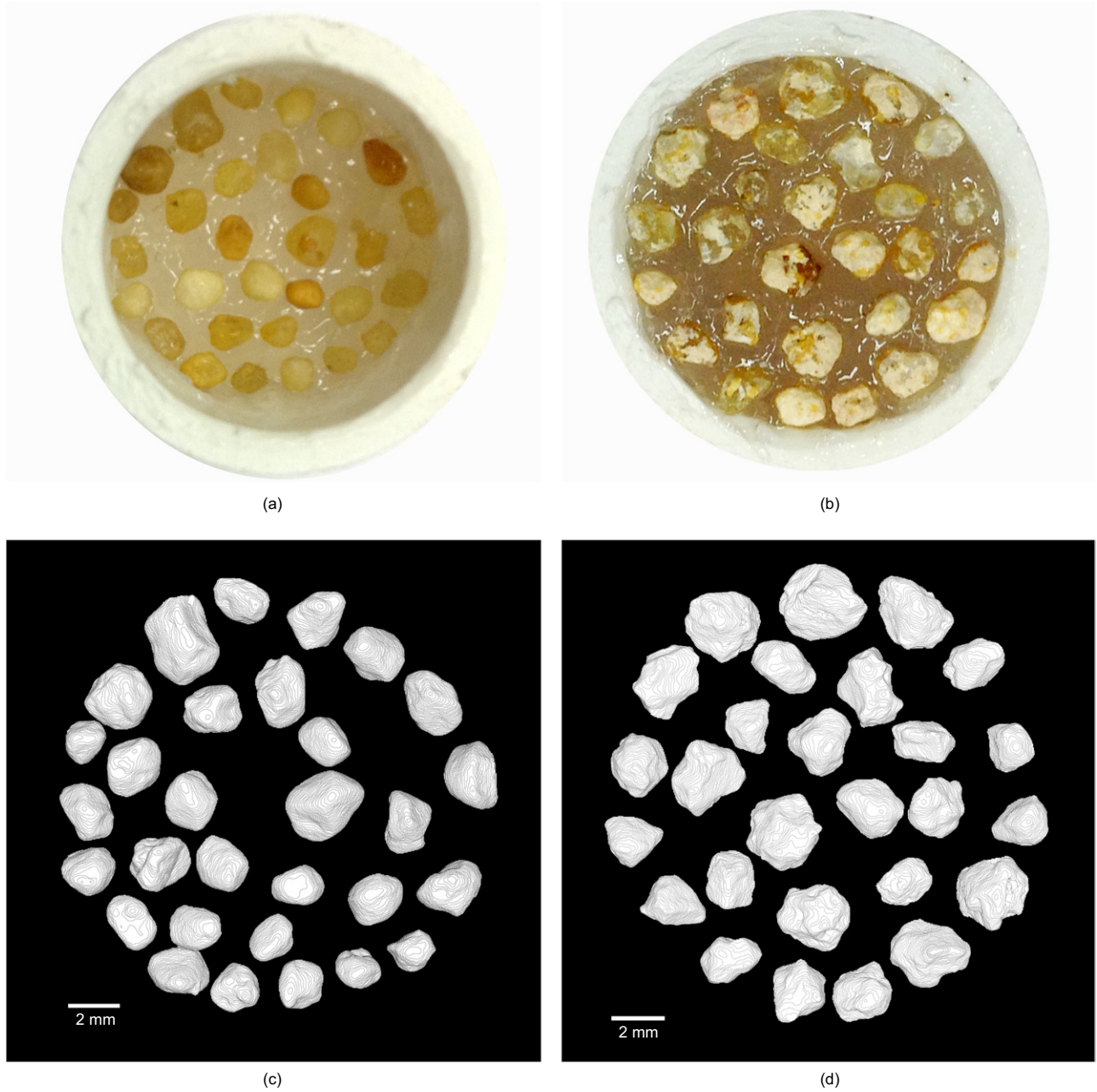


Fig. 1. Scanning specimens and volume rendering of  $\mu$ CT images: (a) a layer of LBS particles; (b) a layer of HDG particles; (c)  $\mu$ CT images of LBS particles; (d)  $\mu$ CT images of HDG particles

sphere to the particle profile composed of the marginal vertices  $(x, y, z)$  and to calculate the associated SH coefficients

$$r(\theta, \phi) = \sum_{n=0}^{\infty} \sum_{m=-n}^n a_n^m Y_n^m(\theta, \phi) \quad (1)$$

where  $r(\theta, \phi)$  is the polar radius from the particle centre with the spherical coordinates  $\theta \in [0, \pi]$  and  $\phi \in [0, 2\pi]$ , which can be obtained by the Cartesian-to-spherical coordinate conversion from  $(x, y, z)$ ;  $Y_n^m(\theta, \phi)$  is the SH series given by equation (2); and  $a_n^m$  is the associated SH coefficient that needs to be determined.

$$Y_n^m(\theta, \phi) = \sqrt{\frac{(2n+1)(n-m)!}{4\pi(n+m)!}} P_n^m(\cos \theta) e^{im\phi} \quad (2)$$

where  $P_n^m(x)$  are the associated Legendre polynomials defined by the differential equation

$$P_n^m(x) = \frac{(-1)^m}{2^n n!} (1-x^2)^{m/2} \frac{d^{n+m}}{dx^{n+m}} (x^2-1)^n \quad (3)$$

where  $n$  and  $m$  are the degree and order of  $P_n^m(x)$ , respectively. Note that  $n$  is a non-negative integer from zero to infinity according to the required fitting precision, and thus the total number of one set of  $a_n^m$  is  $(n+1)^2$ .

Taking  $r(\theta, \phi)$  as the input on the left side of equation (1), a linear system of equations is obtained with  $(n+1)^2$  unknowns. The authors (Zhou & Wang, 2015, 2017) have already proven that SH analysis is sufficient (i.e. the local error is less than 2% at the  $\mu$ CT scanning scale) to represent the local morphological features (i.e. local roundness and surface textures) of the particle surface when the maximum

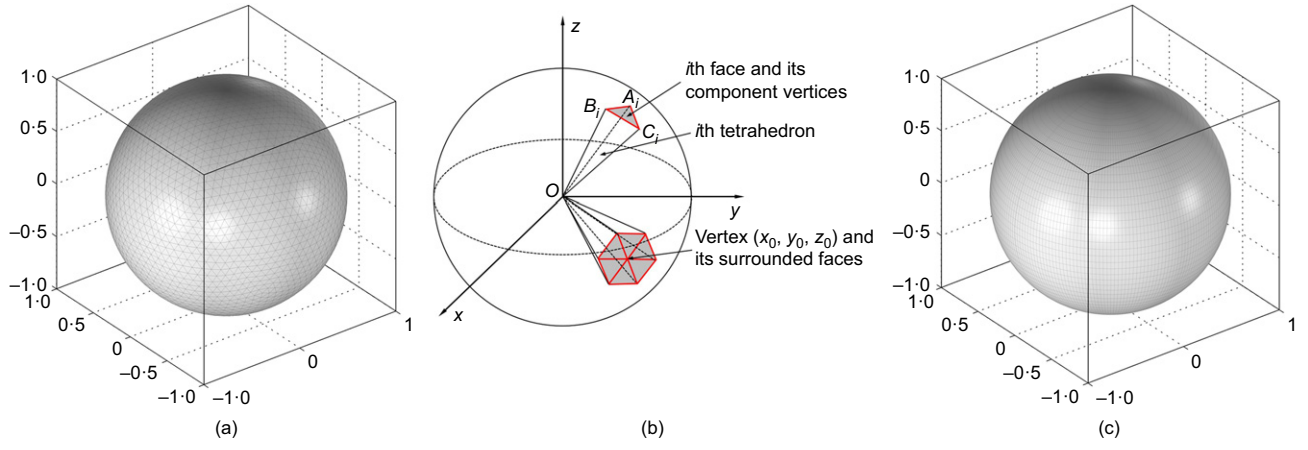


Fig. 2. (a) Subdivided-triangular mapping mesh with 10 240 vertices and 20 480 faces; and (b) diagram of the calculating principals of the volume, surface area and local curvature of the particle based on the subdivided-triangular mapping mesh; (c) subdivided-quadrangular mapping mesh with 160 000 vertices and 159 201 faces

SH degree is greater than 15. With the current  $\mu$ CT resolution, the number of surface vertices is approximately 20 000, which is large enough to uniquely solve this equation system. Adopting the standard least-squares estimation, it is easy to determine its optimised solution of  $a_n^m$ . Note that this set of  $a_n^m$  includes all complex numbers due to the properties of the associated Legendre polynomials. By using the obtained  $a_n^m$  and a mapping spherical mesh (see Fig. 2), it is possible to reconstruct the continuous fitting surface of the

particle by using

$$\hat{r}(\theta, \phi) = \sum_{n=0}^{n_{\max}} \sum_{m=-n}^n a_n^m Y_n^m(\theta, \phi) \quad (4)$$

The maximum SH degree  $n_{\max}$  was set to 20, and two kinds of high-precision mapping meshes (i.e. Figs 2(a) and 2(c)) were used to ensure the accuracy of the SH-reconstructed particle surface. Fig. 3 shows the volume visualisation of the  $\mu$ CT

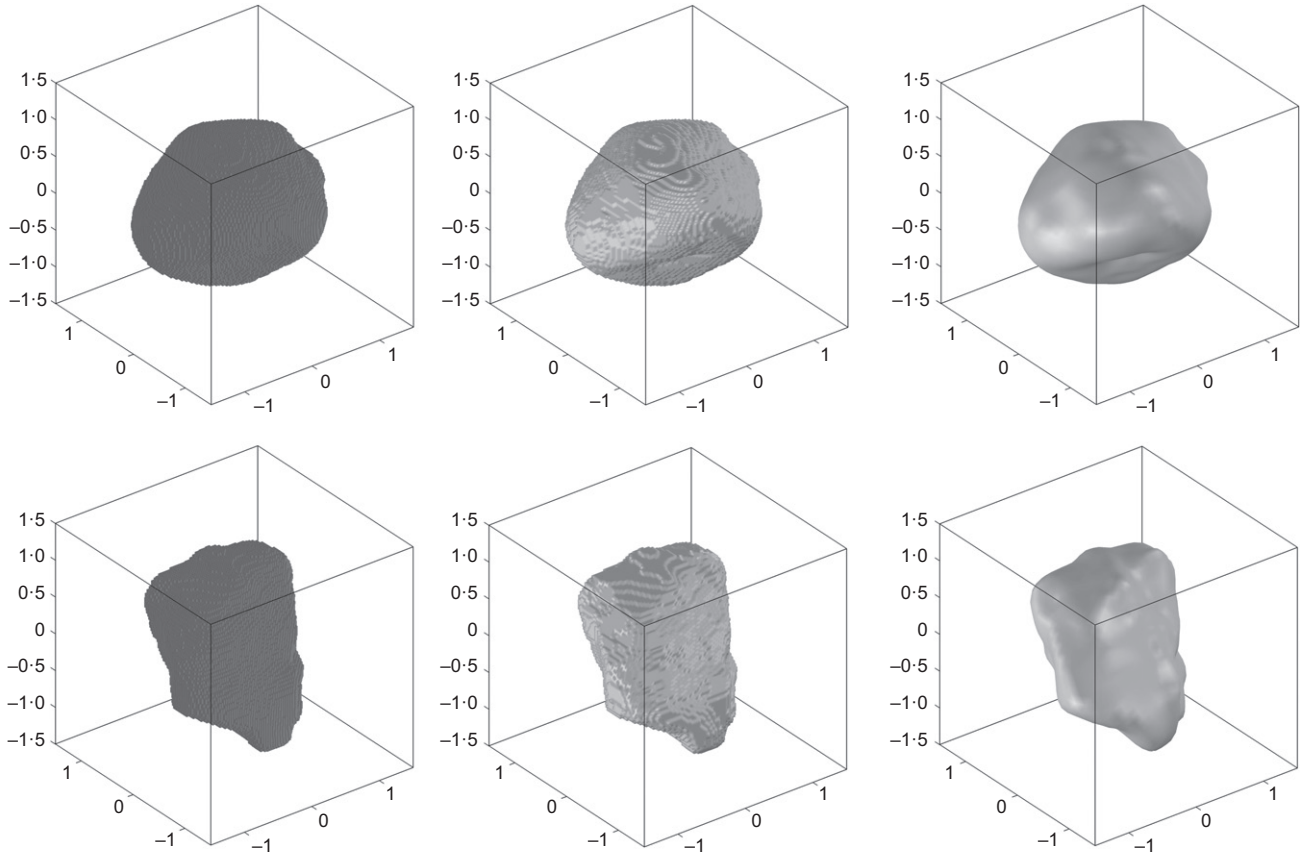


Fig. 3. Volume visualisation of  $\mu$ CT images, voxel-based surface reconstruction and SH-based surface reconstruction of a typical LBS particle and a typical HDG particle



images, voxel-based surface reconstruction and SH-based surface reconstruction of a typical LBS particle and a typical HDG particle. It can be clearly seen that the voxel-based surface contains many jagged stair-steps, whereas the SH-based surface possesses smooth and continuous characteristics. From visual inspection, the morphological features of the SH-reconstructed surface agree well with the microscopic view of the sand particle in Figs 1(a) and 1(b). According to previous findings by the authors, the SH-reconstructed surface has three major advantages: (a) it is a progressive accumulation of surface textures; (b) it is a global optimisation to minimise the error to the original particle surface; and (c) it has the characteristics of the SH function, including continuity and differentiability.

## MORPHOLOGICAL DESCRIPTORS OF SAND PARTICLES

### Three-dimensional sphericity

The commonly used sphericity definition first proposed by Wadell (1935) indicates the ratio of the surface area of a sphere with the same volume as the given particle to the surface area of the particle, as expressed by

$$S = \frac{\sqrt[3]{36\pi V^2}}{SA} \quad (5)$$

where  $S$  is the 3D sphericity of the given particle, and  $V$  and  $SA$  are the volume and the surface area of the given particle, respectively.

Using equation (5), it is easy to calculate the 3D sphericity of a given particle if its accurate volume and surface area are obtained. To calculate the particle's volume and surface area, two methods are introduced based on image analysis and SH analysis, respectively. Based on image analysis of the  $\mu$ CT images, the volume and the surface area can be easily obtained by counting the number of total voxels and boundary voxels, respectively. With regard to SH analysis, many studies have focused on the mathematical calculations of its geometrical properties, including volume, surface area, inertia of the moment and surface curvature (Garboczi, 2002; Bullard & Garboczi, 2013; Zhou *et al.*, 2015). However, these mathematical calculations have always involved complicated derivations and large computations. Hence, the present authors proposed a simple and practical method based on the SH-reconstructed surface mesh to calculate the particle's volume, surface area and local surface curvature. In this and the following section, the subdivided triangular mesh (see Fig. 2(a)) is used as the mapping spherical mesh of the SH reconstruction. As illustrated in Fig. 2(b), the particle's surface area and volume are the sum of the micro-surface area of all faces and the sum of the micro-volume of all tetrahedrons, which can be expressed by

$$SA = \sum_i \frac{1}{2} \left| \overrightarrow{A_i B_i} \times \overrightarrow{B_i C_i} \right| \quad (6)$$

$$V = \sum_i \frac{1}{6} \left| \overrightarrow{OA_i} \cdot \left( \overrightarrow{OB_i} \times \overrightarrow{OC_i} \right) \right| \quad (7)$$

where  $O$  is the centre of the particle and  $A_i$ ,  $B_i$  and  $C_i$  are the component vertices of the  $i$ th face of the surface mesh.

To validate the efficiency of these two methods, a unit octahedron and an ellipsoid with principal dimensions of 2, 1 and 1 mm were selected to calculate their volume and surface area. Fig. 4(a) shows the evolution of the particle volume from the CT reconstruction and the SH

reconstruction with the increasing voxel resolution and SH degree. The results obtained with both methods rapidly converge to the theoretical value as the voxel resolution and SH degree increase. Therefore, it can be concluded that both methods are capable of accurately calculating the volume of particles if the voxel resolution and the SH degree are sufficiently high. This result also proves the efficiency of SH reconstruction in representing the particle morphology.

To calculate the particle surface area by image analysis, the boundary voxels should first be identified with the boundary-detection algorithm combined with voxel connectivity criterion. In image analysis, there are three typical connectivities or neighbourhood relations between 3D voxels. The terms six-, 18- and 26-connectivity are used according to the number of voxels that have a common face, common edge or common vertex with a given voxel, respectively (Fonseca, 2011). To investigate the influence of voxel resolution and voxel connectivity on the calculated surface area, Figs 4(b) and 4(c) present the development of the calculated surface area of ideal particles (i.e. the unit octahedron and the ellipsoid) and real sand particles (i.e. the LBS particle and HDG particle in Fig. 3, respectively). The surface area calculated by image analysis observably increases as the voxel resolution and connectivity order increase, especially in the latter case. Specifically, in Fig. 4(b), most of the image analysis results deviate from the theoretical value of the surface area. With regard to SH analysis, the results gradually converge to a stable value for both ideal particles and real sand particles. The stable results for ideal particles agree well with their theoretical values. Fig. 3 demonstrates the reason why SH analysis instead of image analysis can obtain a reasonable particle surface area. The boundary voxels detected by higher-order connectivity are highly overlapping, which always results in an overestimation of the calculated surface area. Consequently, the surface area calculated by image analysis is highly sensitive to the connectivity order, as shown in Figs 4(b) and 4(c). For this reason, Fonseca (2011) suggested that lower-order connectivity should be used for highly complex and irregular particles to avoid overestimation of the surface area. In contrast, for the SH-reconstructed surface, it optimally fits the original particle profile and retains the smooth and continuous properties of the real particle surface at this observation scale. Two major conclusions can be drawn: (a) the measurement of surface area by image analysis is uncertain and (b) the measurement of surface area by SH analysis is able to achieve a reasonable result when the SH degree is sufficiently high.

To calibrate the surface area calculated by image analysis, Fig. 5 plots the correlation between the results of the surface area of sand particles by SH analysis and by image analysis. A linear correlation can be clearly observed for the particles in which different slopes are obtained for different connectivities. Therefore, the calibration of the image-based surface area ( $SA_{\text{image}}$ ) of these two types of sand particles can be expressed by

$$SA_{\text{image}} = \alpha SA_{\text{SH}} \quad (8)$$

where  $\alpha$  is the correction coefficient that is the reciprocal of the line slope in Fig. 5. For LBS and HDG particles, the  $\alpha$  value is 1.08 and 1.2 for six-connectivity, 0.71 and 0.79 for 18-connectivity and 0.62 and 0.68 for 26-connectivity, respectively. Once the correct volume and surface area of the particle are determined, the accurate 3D sphericity of this particle can be easily obtained with equation (5).

### Three-dimensional roundness

According to Wadell (1935) and Blott & Pye (2008), 2D roundness is quantified by the average ratio of the curvature

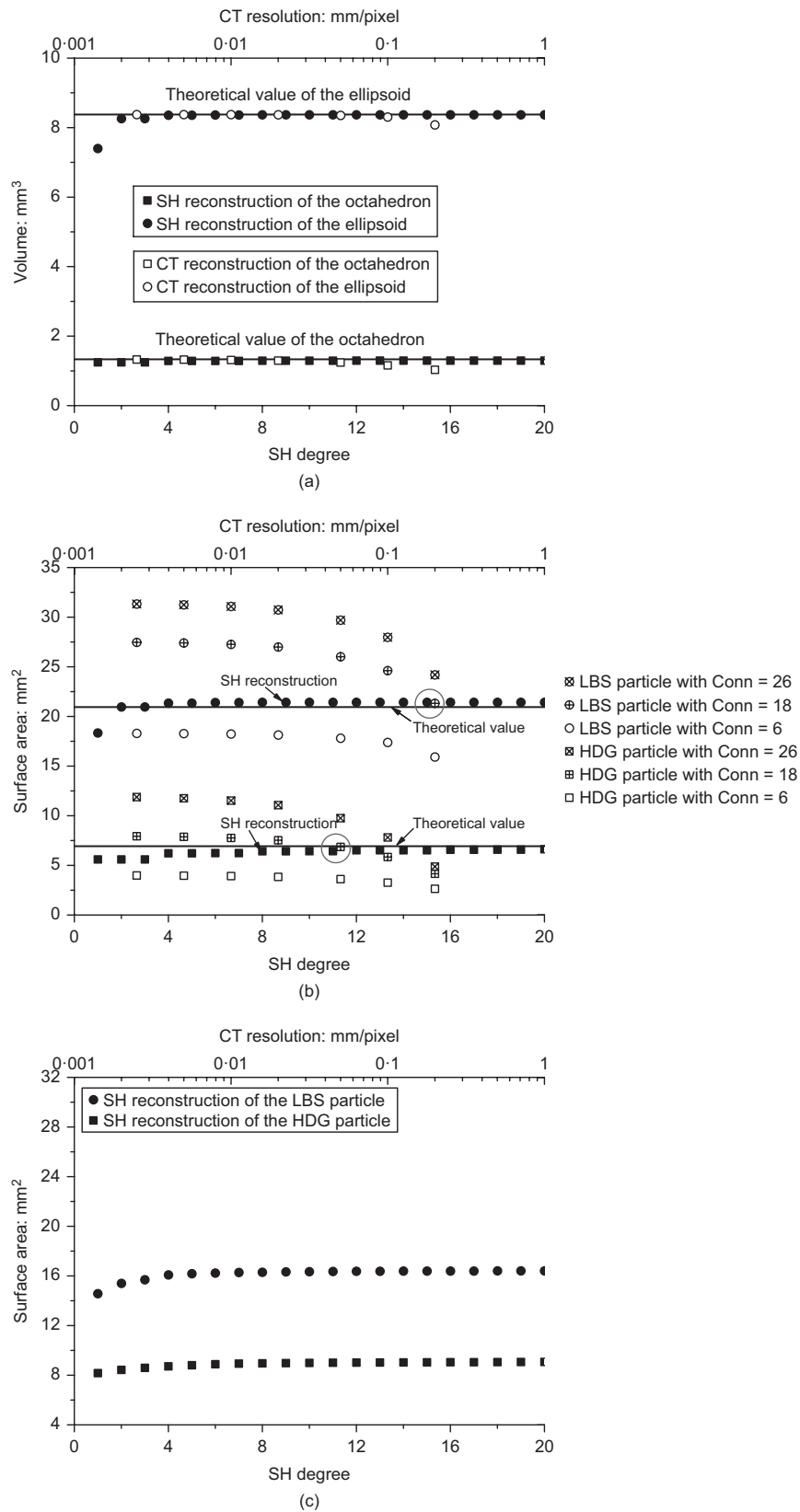


**Fig. 4. Development of particle volume and surface area based on image analysis and SH analysis with an increase in the voxel resolution and SH degree: (a) calculated particle volume of ideal particles (i.e. the unit octahedron and the ellipsoid); (b) calculated surface area of ideal particles; (c) calculated surface area of real sand particles (i.e. the LBS particle and the HDG particle in Fig. 3)**

radius of all corners to the radius of the largest inscribed circle of a particle. However, the curvature of a regular 3D surface measured at a given point depends on the path through the point, which means that a unique curvature at a

given point does not exist. For this reason, based on the understanding of the surface curvature, the introduction of a reasonable definition of the 'corner' on the particle surface and its characteristic index was necessary in this study.

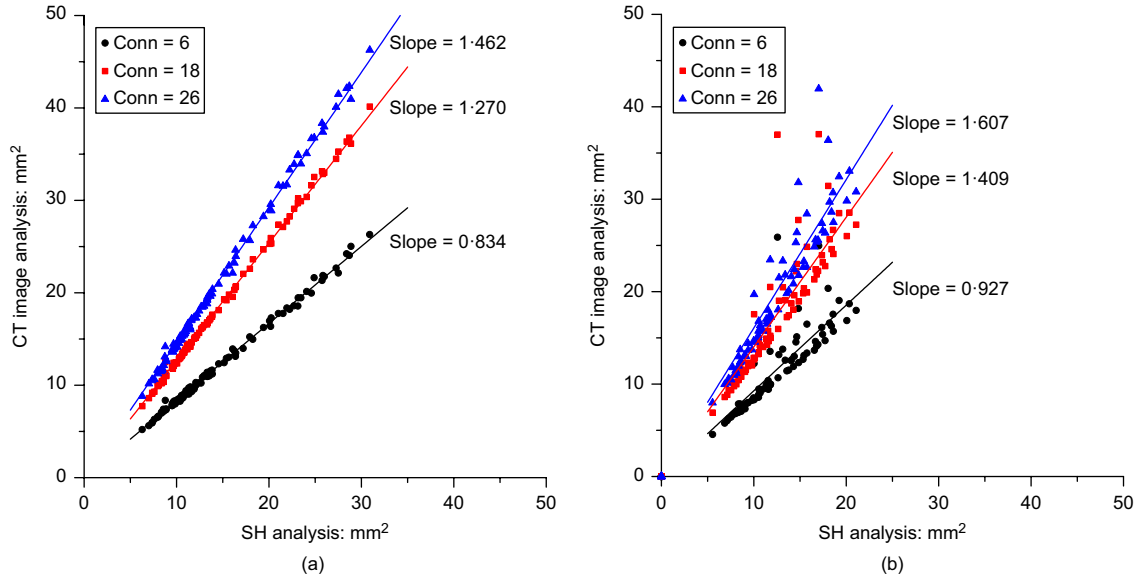


Fig. 5. Correlation between the results of the surface area by SH analysis and by image analysis: (a) LBS particles; (b) HDG particles

Generally, two principal curvatures, that is, the maximum and the minimum of the normal curvatures  $\kappa_{\max}$  and  $\kappa_{\min}$ , were commonly used to measure the maximum and minimum bending of a surface at a given point (Do Carmo, 1976). The perpendicular directions of the paths that hold the principal curvatures are called the principal directions, and the inverses  $r_{\max} = 1/\kappa_{\min}$  and  $r_{\min} = 1/\kappa_{\max}$  are the principal curvature radii. In this study, the authors introduced a practical approach proposed by Colombo *et al.* (2006) to measure the local principal curvatures at a given vertex  $(x_0, y_0, z_0)$  on the SH-reconstructed surface. The key idea of this approach is to generate a local micro-surface made of first-ring adjacent faces of this given vertex, as illustrated in Fig. 2(b), and to establish a biquadratic polynomial function to approximate this micro-surface, as expressed by

$$z = f(x, y) \approx a + b(x - x_0) + c(y - y_0) + d(x - x_0)(y - y_0) + e(x - x_0)^2 + g(y - y_0)^2 \quad (9)$$

where  $a, b, c, d, e$  and  $g$  are the unknown coefficients that need to be determined.

Because there are seven vertices inside the micro-surface forming the input of this function, it is easy to calculate these six unknowns using the least-squares fitting method. The shape characteristics of the micro-surface at this given vertex can be described by the  $2 \times 2$  Hessian matrix (Do Carmo, 1976), as expressed by equation (10). The principal curvatures and principal directions are the eigenvalues and eigenvectors of this Hessian matrix, respectively.

$$H(x_0, y_0) = \begin{bmatrix} f_{xx}(x_0, y_0) & f_{xy}(x_0, y_0) \\ f_{yx}(x_0, y_0) & f_{yy}(x_0, y_0) \end{bmatrix} \quad (10)$$

where  $f_{xx}, f_{xy}, f_{yx}$  and  $f_{yy}$  are the second derivatives of  $f(x, y)$  in equation (9), in which  $f_{xx}(x_0, y_0) = 2e$ ,  $f_{xy}(x_0, y_0) = f_{yx}(x_0, y_0) = d$  and  $f_{yy}(x_0, y_0) = 2g$ .

Figure 6 shows the contours of  $\kappa_{\max}$  and  $\kappa_{\min}$  of the unit octahedron and the LBS and HDG particles in Fig. 3. Take the unit octahedron for illustration, the principal curvatures at any vertex on the plane are  $\kappa_{\max} = \kappa_{\min} = 0$ , and the curvature radii are  $r_{\min} = r_{\max} = \infty$ . Therefore, no ‘corners’ can be defined on the planes. Imagine placing a slightly rounded edge along one edge of an octahedron to connect its

two conjoint planes, the principal curvatures are  $\kappa_{\min} = 0$  and  $\kappa_{\max}$  (where  $\kappa_{\max}$  is a real number that depends on the size of the rounded edge) along the edge direction and perpendicular to the edge direction, respectively. The corresponding curvature radii are  $r_{\max} = \infty$  and  $r_{\min} = 1/\kappa_{\max}$ , respectively. From a natural understanding of the meaning of the ‘corner’ of an edge,  $r_{\min}$  is a reasonable index to characterise the curvature radius of this kind of ‘corner’. Furthermore, for the sand particles in Fig. 6,  $\kappa_{\max}$  is much more distinguishable than  $\kappa_{\min}$  to identify the ‘corners’. Consequently, the curvature radius  $r_{\min} = |\kappa_{\max}|^{-1}$  was used to characterise a potential ‘corner’ at a given vertex on the surface and defined the ‘corner’ by

$$g(\kappa) = \begin{cases} 1 & \text{if } |\kappa_{\max}|^{-1} < R_{\text{ins}} \\ 0 & \text{if } |\kappa_{\max}|^{-1} \geq R_{\text{ins}} \end{cases} \quad (11)$$

where 1 or 0 indicates that the ‘corner’ is acceptable or unacceptable, respectively, and  $R_{\text{ins}}$  is the radius of the maximum inscribed sphere of the particle, which is precisely the minimum polar radius in equation (4). The 3D roundness of the particle can then be obtained by

$$R = \frac{\sum g(\kappa) |\kappa_{\max}|^{-1}}{NR_{\text{ins}}} \quad (12)$$

where  $N$  is the total number of acceptable ‘corners’.

### Three-dimensional fractal dimension

Hyslip & Vallejo (1997) first developed 2D fractal geometry to characterise and quantify irregular and fragmented patterns within natural sand particles. The idea is to use different yardsticks to measure the perimeter of the profile extracted from the 2D particle projection and evaluate the fractal dimension based on the relationship between the yardsticks and the measured perimeters in log-log scale. With regard to a 3D open surface (e.g. the fracture surface and topographic surface), the triangular prism method (TPM) first proposed by Clarke (1986) and the slit island method (SIM) first proposed by Mandelbrot *et al.* (1984) have been widely applied to evaluate the 3D fractal dimension. With the TPM, the plane projection of the fracture surface is divided into uniform squares with different

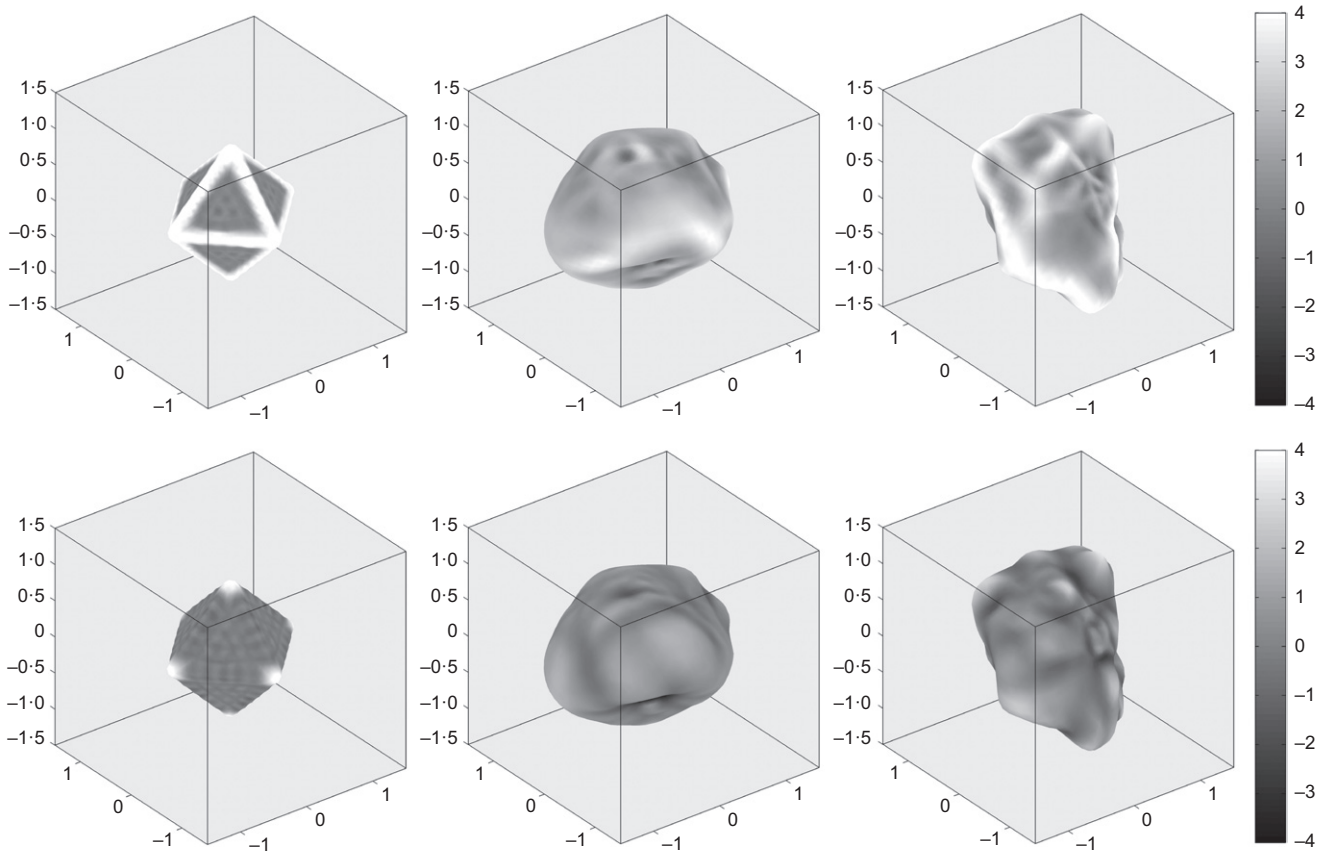


Fig. 6. Contours of  $\kappa_{\max}$  and  $\kappa_{\min}$  of the unit octahedron and the LBS and HDG particles in Fig. 3

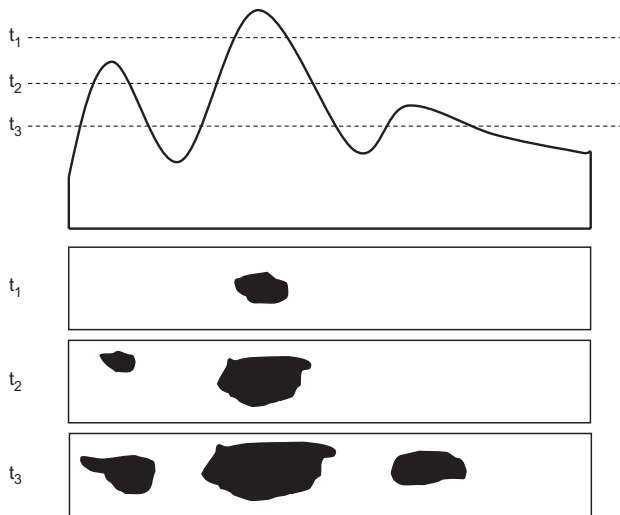


Fig. 7. Diagram of the procedures of the slit island method (Charkaluk *et al.*, 1998).  $t_1$ ,  $t_2$  and  $t_3$  represent the evolution of the slit 'islands' (i.e. black regions) and 'lakes' (i.e. white regions) with increasing polishing times

sizes, and the associated surface area is then calculated. Within the SIM, the fractured specimen is first mounted in a resin plane base. The next step consists of careful polishing of the fracture surface parallel to the plane base to highlight the material 'islands' surrounded by air 'lakes', as illustrated in Fig. 7. Charkaluk *et al.* (1998) and Yuan *et al.* (2003) found that the relationship between the perimeter  $P$  and area  $A$  of the 'islands' represents the fractal nature well, which can be

expressed by

$$P^{1/d} \propto A^{1/2} \quad (13)$$

where  $d$  is the fractal dimensional increment. The converting form of this function is

$$\log P = 0.5d \log A + C \quad (14)$$

where  $C$  is a constant. Therefore, the fractal dimension of a fractured surface is

$$D = d + 1 \quad (15)$$

However, the TPM and SIM are not capable of calculating the fractal dimension of the 3D closed surface, such as a sand particle surface. No plane projection can cover the full morphological information of the 3D closed surface using the TPM. Similarly, by using the SIM, there might be only one 'island' and no neighbouring 'lake', regardless of the polishing degree. For this reason, the present authors attempted to develop a novel method based on the idea of the SIM to evaluate the 3D fractal dimension of the 3D closed surface of sand particles. For an open surface, SIM captures the 'islands' and 'lakes' from the polishing planes parallel to the base. For a closed surface, a similar idea was followed to polish the particle spherically and produce a series of 'islands' and 'lakes' on the spherical polishing surface. In practice, a spherical surface was expanded from the maximum inscribed sphere to the minimum circumscribed sphere of a given particle to intersect the particle profile in the spherical coordinate space. The portion of the particle outside this spherical surface was polished to produce a series of 'islands' surrounded by 'lakes' or a series of 'lakes' surrounded by 'islands' on the spherical surface. These 'islands' and 'lakes' carry the morphological



information of the surface texture and roughness. By calculating the perimeters and the areas of the 'islands' or 'lakes' subject to different polishing degrees, it is possible to estimate the 3D fractal dimension of the real particle morphology according to equations (14) and (15).

The major difficulty in this method is to identify the individual 'islands' and 'lakes' on the spherical polishing surface. To overcome this difficulty, a novel method, 'image projection analysis' (IPA), is proposed in this section. The key idea of IPA is to project the spherical polishing surface to a binary image and then identify the closed boundaries and their corresponding regions (i.e. 'islands' or 'lakes') with image-processing techniques. Figure 8 illustrates the flow chart to calculate the 3D fractal dimension of the particle morphology. The flow chart includes two main parts: the polishing and geometry calculation part with solid line blocks and the IPA part with dashed line blocks. Following this flow chart, the calculation process of the 3D fractal dimension is described in detail as follows.

First, the 3D particle surface was generated by the high-level SH reconstruction discussed in the earlier section entitled 'Spherical harmonic reconstruction of particle surface'. To implement the IPA, a subdivided quadrangular mesh, instead of a subdivided triangular mesh, was chosen as the mapping spherical mesh, as shown in Fig. 2(c). To

ensure the resolution of the projected image, the spherical coordinate matrix used in this section was  $400 \times 400$ . Similarly to  $R_{ins}$ , it is also easy to determine the radius of the minimum circumscribed sphere ( $R_{cir}$ ) of the particle that is the maximum polar radius in equation (4). A spherical surface was then continuously expanded to intersect the particle surface (to imitate the polishing procedures) to produce a series of 'islands' and 'lakes' (i.e. the regions inside the intersecting line boundaries) on this spherical surface, as illustrated in the first row of Fig. 9.

To identify the individual boundaries and their containing regions (i.e. 'islands' or 'lakes') on the intersecting spherical surface, the intersected particle surface was projected to a binary image in which the location of a pixel corresponds to the spherical coordinate of a vertex, and the grey level of this pixel was initialised as one or zero if this vertex lay outside or inside the intersecting spherical surface, respectively, as demonstrated in the second row of Fig. 9. By using the intrinsic function edge in Matlab, each of the edge pixels in this image can be detected to produce a binary edge-image in which the grey levels of the edge pixels and the background pixels are set to one and zero, respectively, as shown in the third row of Fig. 9. To separate the individual boundaries, the intrinsic function 'bwlabel' in Matlab was applied to this edge-image. In addition, the individual boundaries can be identified and labelled with a set of connected edge pixels with the same grey levels. For each individual boundary, a new binary image was initialised in which the grey level of the constituent edge pixels and the background pixels were set to zero and one, respectively. The function 'bwlabel' was again applied to identify the two individual parts of this image. It was determined that the smaller part is exactly the region that belongs to this boundary, as demonstrated in Fig. 10. This definition can be easily understood by imagining that a closed curve on a spherical surface divides this spherical surface into two parts. It is then reasonable to regard the smaller part and the larger part as its internal region and external region, respectively. If the number of total pixels within the identified region was larger than three, the boundary pixels and region pixels were projected back to the spherical coordinate space, and the corresponding boundary vertices and the faces belonging to this boundary could finally be determined.

By implementing the above steps, Fig. 10 plots the boundaries (i.e. the intersecting lines that consist of the detected boundary vertices) and the regions (i.e. the grey curved surface that consists of the detected faces) of the identified individual 'islands' on the tenth intersecting spherical surface in Fig. 9. It is easy to calculate the perimeter and area of an 'island' based on its boundary vertices and belonging faces in 3D Cartesian coordinate space. Finally, it is possible to investigate the correlation between the total perimeter and total area of each of the identified 'islands' or 'lakes' on different intersecting spherical surfaces at log-log scale and evaluate the 3D fractal dimension of the particle morphology. Fig. 11 shows the relationship between the obtained perimeter and area in log-log scale and the calculated 3D fractal dimension for an ellipsoid, a virtual star particle and the LBS and HDG particles in Fig. 3. The powerful law can be clearly observed for all of the particles. The fractal dimension of the ellipsoid is 2.0, which means that no textures or roughness details can be captured on its surface. The increase in the fractal dimension indicates the increase of the surface textures and roughness details of the particle. For the selected particles in Fig. 11, the virtual star particle with numerous projections has the largest fractal dimension of 2.616, and the fractal dimension of the HDG particle is slightly larger than that of the LBS particle.

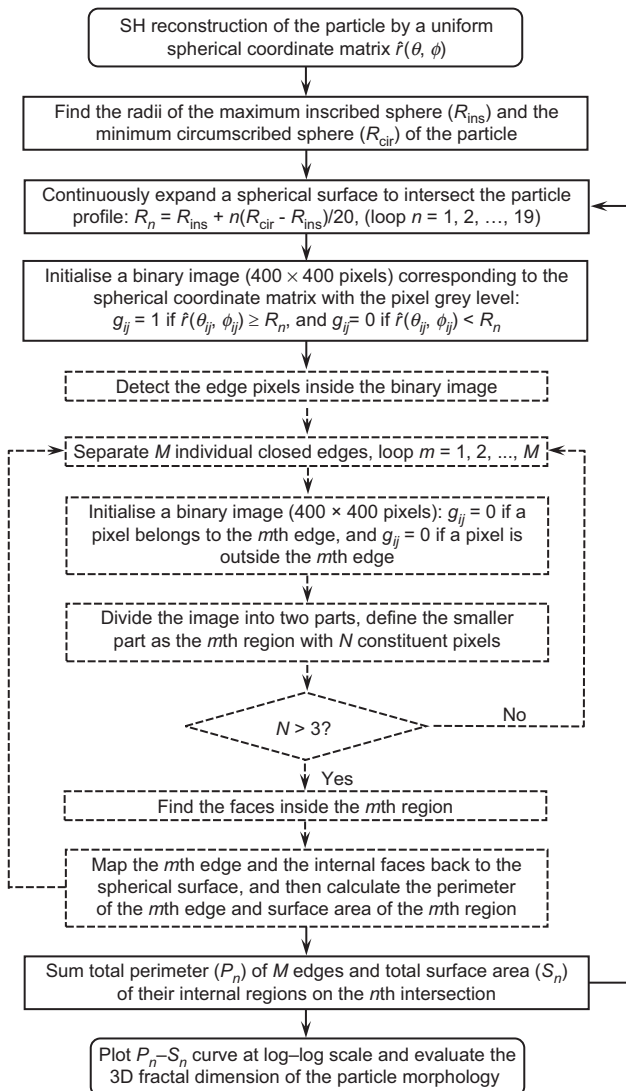


Fig. 8. Flow chart for calculating the 3D fractal dimension

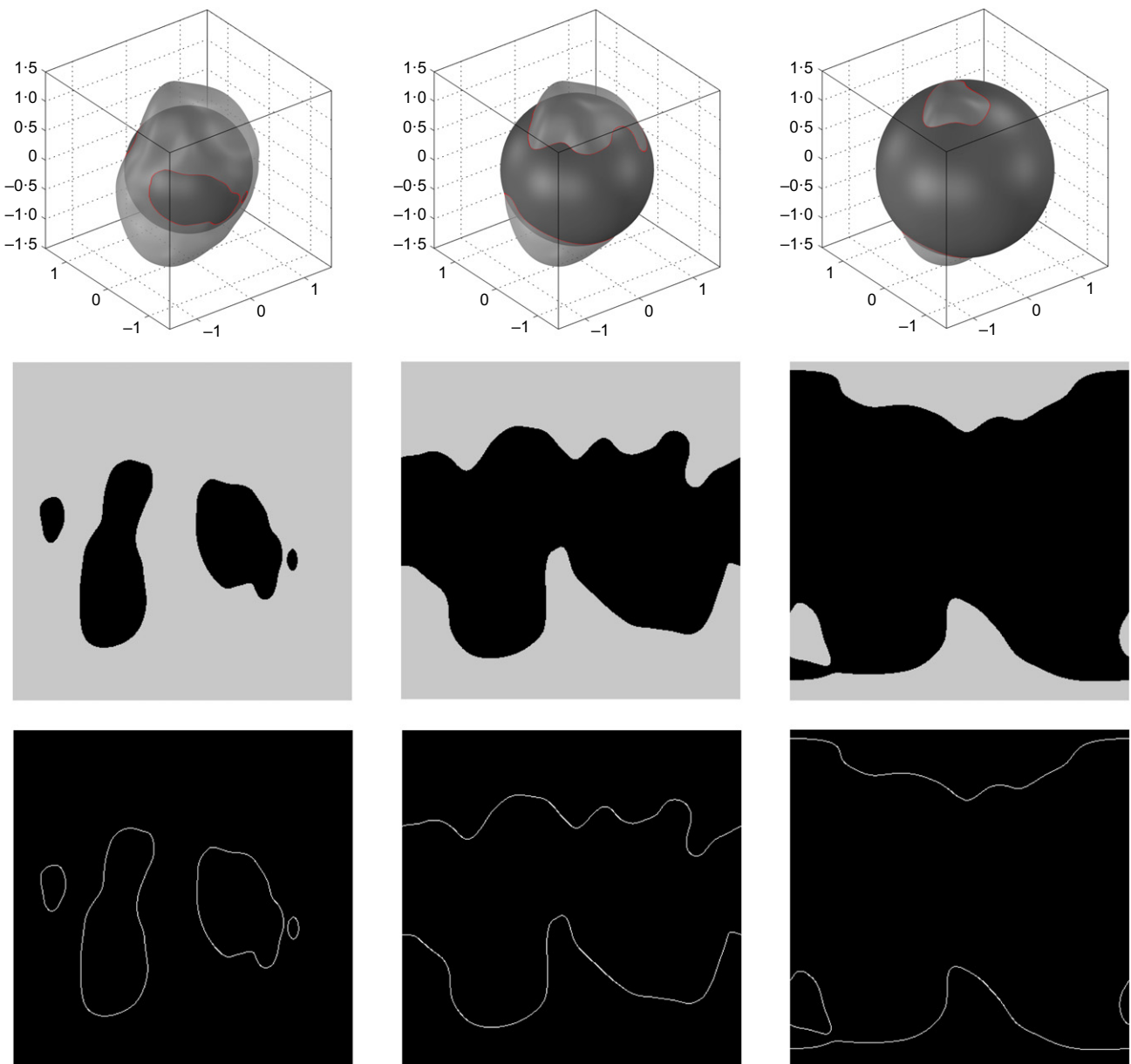


Fig. 9. Identification of the individual boundaries on the fifth, tenth and 15th intersected spherical surfaces

## RESULTS AND DISCUSSION

According to the proposed calculation methods in the previous section ‘Morphological descriptors of sand particles’, the 3D sphericity, roundness and fractal dimension of real LBS and HDG particles can be obtained. The statistics and correlation of these morphological descriptors are investigated in the present section. The statistical indices of the results for 120 LBS particles and 80 HDG particles are summarised in Table 1. As expected, the HDG particles have lower mean values and higher standard deviations of sphericity and roundness than the LBS particles, which again proves that the particle morphology of HDG is more irregular and angular than that of LBS. With regard to fractal dimension, the mean value and the standard deviation of the HDG particles are higher than those of the LBS particles. This indicates that the surface textures of the HDG particles are rougher and more complex than those of LBS particles.

Figure 12 further shows the correlation between these 3D morphological descriptors. On the whole, a correlation can

be observed in any subfigure, which indicates that the morphological features of the particle at different scales are not independent. Specifically, two relatively high correlation coefficients of 0.415 and 0.424 were obtained between sphericity and roundness and between roundness and fractal dimension, respectively. This result agrees well with the results of Fonseca *et al.* (2012) and Zhao & Wang (2016), who found a strong correlation between the sphericity and the convexity and roundness of sand particles. The relatively high correlation between the roundness and the fractal dimension is mainly because no definitive boundary exists between the scales of local corners and surface textures of sand particles (Soga & Mitchell, 2005). In contrast, a relatively low correlation coefficient of 0.179 was obtained between sphericity and fractal dimension, probably because sphericity describes the general form of the particle on a large scale, whereas the fractal dimension characterises the surface texture and roughness at fine scales. These results suggest that the correlation between any two morphological descriptors depends on the distance between their characteristic scales.

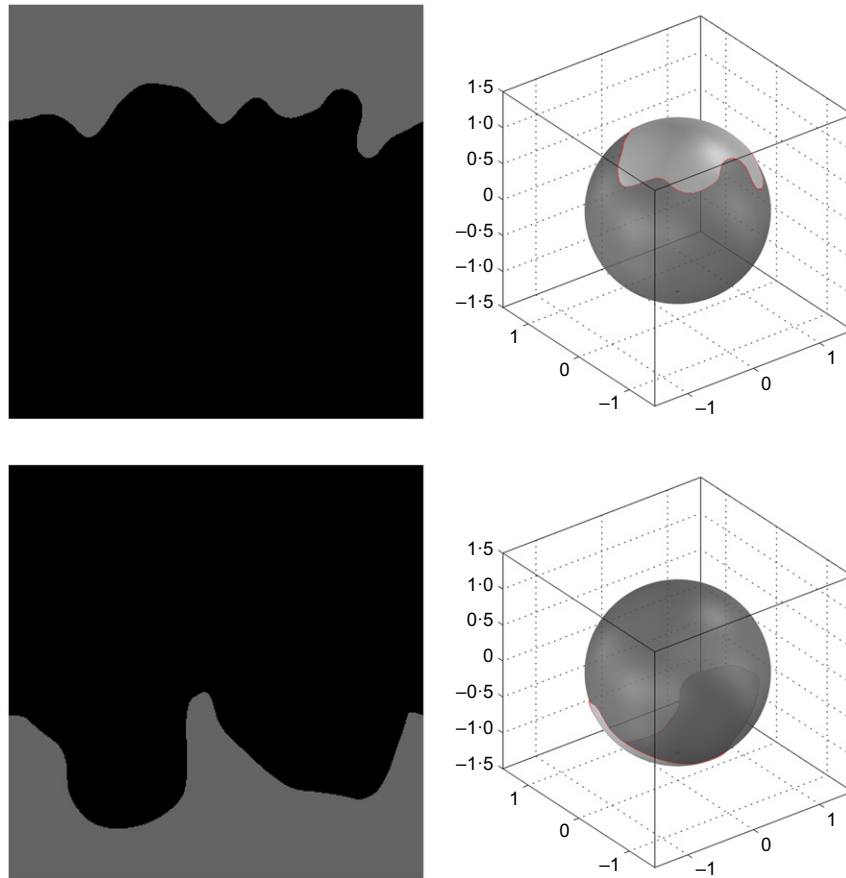


Fig. 10. Identified individual boundaries and their internal regions on the tenth intersected spherical surface

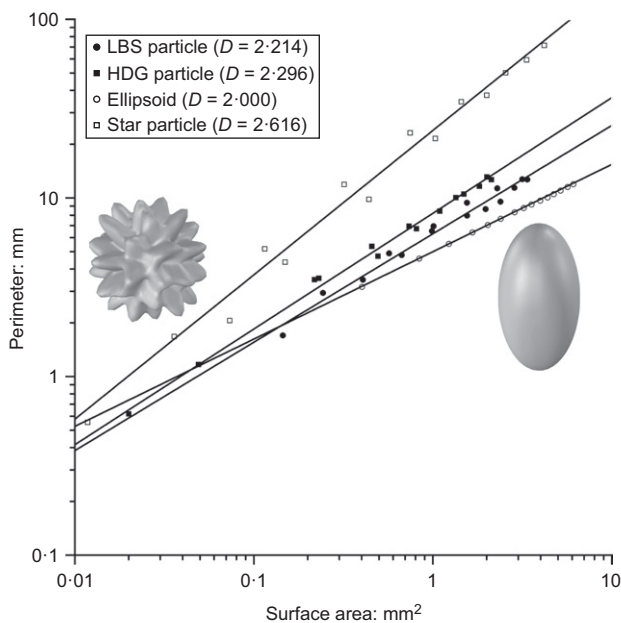


Fig. 11. Relationship between the perimeter and area in log-log scale and the calculated 3D fractal dimension for an ellipsoid, a virtual star particle, and the LBS and HDG particles in Fig. 3

## CONCLUSIONS

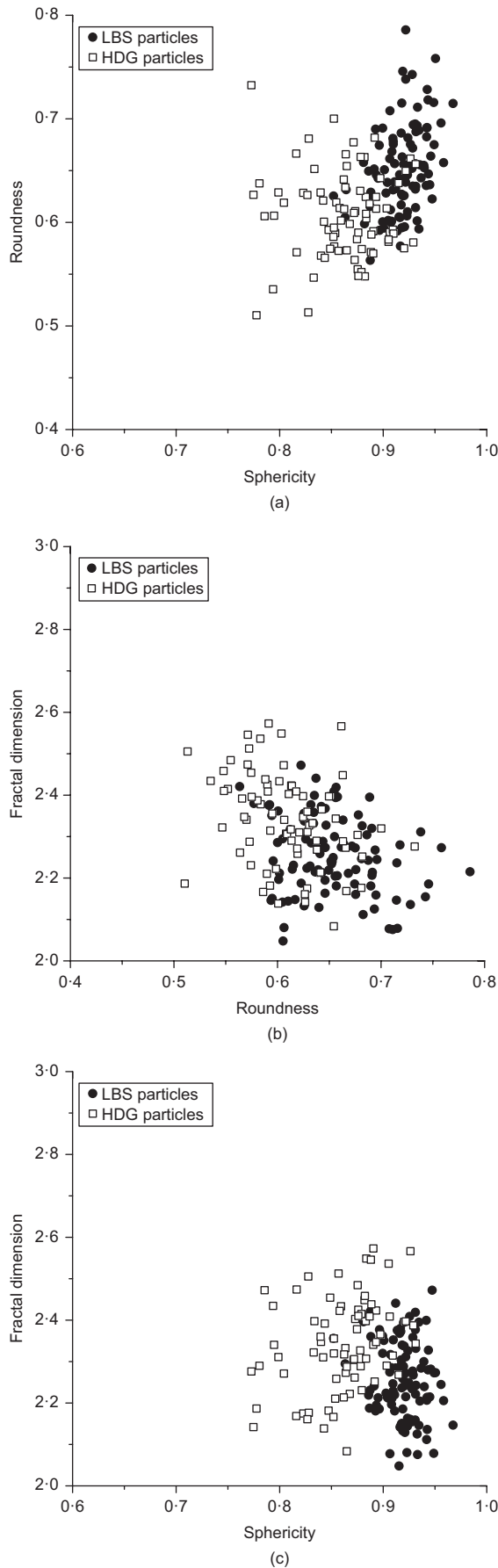
Based on  $\mu$ CT scanning of sand particles and their SH-reconstructed surfaces, this study first developed practical methods to calculate the 3D sphericity and roundness of particles. To calculate 3D sphericity, the surface area

Table 1. Statistics of the 3D morphological descriptors of sand particles

3D descriptors	LBS particles		HDG particles	
	Mean value	Standard deviation	Mean value	Standard deviation
Sphericity	0.918	0.016	0.862	0.030
Roundness	0.652	0.032	0.608	0.036
Fractal dimension	2.239	0.087	2.357	0.117

obtained by image analysis and by SH analysis was carefully investigated and discussed. The results obtained by SH analysis gradually converge to a reasonable surface area at the scale of  $\mu$ CT resolution, in which the stable value of the calculated surface area with a sufficiently high SH degree can be further used to calibrate the surface area by means of image analysis. To calculate 3D roundness, a practical method was introduced to calculate the surface curvature based on the SH-reconstructed mesh of the particle surface. By understanding the geometric properties of the principal curvatures of different kinds of surfaces, the 3D 'corner' was defined and identified to characterise the local roundness of sand particles. The most significant contribution of this study was the establishment of a novel method to calculate the 3D fractal dimension of real sand particles. It was also innovative to modify the SIM by combining it with the IPA, which allowed the successful calculation of the 3D fractal dimension of closed surfaces for sand particles.

By application to the selected ideal particles and to the  $\mu$ CT-scanned real LBS and HDG particles, the results proved



**Fig. 12. Correlation between the 3D morphological descriptors: (a) sphericity plotted against roundness; (b) roundness plotted against fractal dimension; (c) sphericity plotted against fractal dimension**

the capacity and efficiency of the proposed methods to measure these 3D morphological descriptors. The statistics of 3D sphericity, roundness and fractal dimension quantitatively indicated that the particle morphology of HDG presents greater irregularity, angularity and rougher surface textures than those of LBS. Moreover, by investigating the correlation between these morphological descriptors, it was found that the morphological features at different length scales have certain correlations with each other. The correlation relies heavily upon the distance between the characteristic scales of the morphological descriptors. In conclusion, the methods proposed in this study to measure the 3D morphological descriptors of real sand particles make a valuable contribution to the fundamental understanding of particle morphology and strongly improve the characterisation and classification of natural sands in engineering applications. The results from this study may also contribute to more sophisticated and accurate discrete-element modelling of real sands, in aspects such as achievement of a more accurate estimation of the microscopic interparticle contact parameters (e.g. contact stiffness and friction coefficient) and incorporation of more realistic particle morphologies into more advanced discrete-element methods, such as the granular element method proposed by Andrade *et al.* (2012). Based on this work, the present authors' future research will focus on experimental and numerical studies of the effect of these 3D morphological descriptors on the micro- and macro-mechanical behaviour of granular sands.

#### ACKNOWLEDGEMENTS

This study was supported by research grants nos 51508216, 51379180 and 41372296 from the National Science Foundation of China and by General Research Fund no. CityU 11272916 from the Research Grants Council of the Hong Kong SAR.

#### NOTATION

$A$	surface area of an 'island'
$A_i, B_i, C_i$	component vertices of the $i$ th face
$a_n^m$	spherical harmonic coefficient
$D$	fractal dimension
$d$	fractal dimensional increment
$\mathbf{H}(x_0, y_0)$	Hessian matrix
$m, n$	spherical harmonic order and degree
$N$	total number of acceptable 'corners'
$n_{\max}$	maximum spherical harmonic degree used
$O$	centre of a particle
$P$	perimeter of an 'island'
$P_n^m(x)$	associated Legendre function
$R$	roundness
$R_{\text{cir}}$	radius of minimum circumscribed sphere of a particle
$R_{\text{ins}}$	radius of maximum inscribed sphere of a particle
$r_{\max}, r_{\min}$	maximum and minimum principal curvature radii
$r(\theta, \phi)$	polar radius of the particle surface at $\theta$ and $\phi$
$\hat{r}(\theta, \phi)$	SH-reconstructed polar radius of the particle surface at $\theta$ and $\phi$
$S$	sphericity
$SA_{\text{image}}$	image-based surface area of a particle
$SA_{\text{SH}}$	spherical-harmonic-based surface area of a particle
$V$	volume of a particle
$(x, y, z)$	Cartesian coordinates of particle surface vertices
$Y_n^m(\theta, \phi)$	spherical harmonic series
$\alpha$	correction coefficient of the image-based surface area
$\theta, \phi$	polar angle and azimuthal angle of the spherical coordinates
$\kappa_{\max}, \kappa_{\min}$	maximum and minimum of the normal curvatures

## REFERENCES

- Abbramoff, M., Magalhães, P. & Ram, S. (2004). Image processing with ImageJ. *Biophotonics Int.* **11**, No. 7, 36–42.
- Alshibli, K., Druckrey, A., Al-Raoush, R., Weiskittel, T. & Lavrik, N. (2014). Quantifying morphology of sands using 3D imaging. *J. Mater. Civ. Engng* **27**, No. 10, 04014275.
- Altuhafi, F. & Coop, M. (2011). Changes to particle characteristics associated with the compression of sands. *Géotechnique* **61**, No. 6, 459–471, <http://dx.doi.org/10.1680/geot.9.P114>.
- Altuhafi, F., O'Sullivan, C. & Cavarretta, I. (2012). Analysis of an image-based method to quantify the size and shape of sand particles. *J. Geotech. Geoenviron. Engng* **139**, No. 8, 1290–1307.
- Andrade, J., Lim, K., Avila, C. & Vlahinić, I. (2012). Granular element method for computational particle mechanics. *Comput. Methods Appl. Mech. Engng* **241–244**, 262–274.
- ASTM (2009). ASTM D2488: Standard practice for description and identification of soils (visual-manual procedure). West Conshohocken, PA, USA: ASTM International.
- Blott, S. & Pye, K. (2008). Particle shape: a review and new methods of characterization and classification. *Sedimentology* **55**, No. 1, 31–63.
- Bowman, E. T., Soga, K. & Drummond, W. (2001). Particle shape characterisation using Fourier descriptor analysis. *Géotechnique* **51**, No. 6, 545–554, <http://dx.doi.org/10.1680/geot.2001.51.6.545>.
- Bullard, J. & Garboczi, E. (2013). Defining shape measures for 3D star-shaped particles: sphericity, roundness, and dimensions. *Powder Technol.* **249**, 241–252.
- Charkaluk, E., Bigerelle, M. & Iost, A. (1998). Fractals and fracture. *Engng Fracture Mech.* **61**, No. 1, 119–139.
- Clarke, K. (1986). Computation of the fractal dimension of topographic surfaces using the triangular prism surface area method. *Comput. Geosci.* **12**, No. 5, 713–722.
- Colombo, A., Cusano, C. & Schettini, R. (2006). 3D face detection using curvature analysis. *Pattern Recognition* **39**, No. 3, 444–455.
- Cundall, P. & Strack, O. (1979). A discrete numerical-model for granular assemblies. *Géotechnique* **29**, No. 1, 47–65, <http://dx.doi.org/10.1680/geot.1979.29.1.47>.
- Do Carmo, M. P. (1976). *Differential geometry of curves and surfaces*. Englewood Cliffs, NJ, USA: Prentice-Hall.
- Field, D. (1988). Laplacian smoothing and Delaunay triangulations. *Commun. Appl. Numer. Methods* **4**, No. 6, 709–712.
- Fonseca, J. (2011). *The evolution of morphology and fabric of a sand during shearing*. London, UK: Imperial College London.
- Fonseca, J., O'Sullivan, C., Coop, M. & Lee, P. (2012). Non-invasive characterization of particle morphology of natural sands. *Soils Found.* **52**, No. 4, 712–722.
- Garboczi, E. (2002). Three-dimensional mathematical analysis of particle shape using X-ray tomography and spherical harmonics: application to aggregates used in concrete. *Cement Concrete Res.* **32**, No. 10, 1621–1638.
- Guo, P. & Su, X. (2007). Shear strength, interparticle locking, and dilatancy of granular materials. *Can. Geotech. J.* **44**, No. 5, 579–591.
- Hanaor, D., Ghadiri, M., Chrzanowski, W. & Gan, Y. (2014). Scalable surface area characterization by electrokinetic analysis of complex anion adsorption. *Langmuir* **30**, No. 50, 15143–15152.
- Hanaor, D., Gan, Y., Revay, M., Airey, D. W. & Einav, J. (2016). 3D printable geomaterials. *Géotechnique* **66**, No. 4, 323–332, <http://dx.doi.org/10.1680/jgeot.15.P034>.
- Hyslip, J. & Vallejo, L. (1997). Fractal analysis of the roughness and size distribution of granular materials. *Engng Geol.* **48**, No. 3, 231–244.
- Kobbelt, L., Botsch, M., Schwanecke, U. & Seidel, H. (2001). Feature sensitive surface extraction from volume data. In *Proceedings of the 28th annual conference on computer graphics and interactive techniques*, Los Angeles, CA, USA, pp. 57–66.
- Krumbein, W. C. & Sloss, L. L. (1963). *Stratigraphy and sedimentation*, 2nd edn. San Francisco, CA, USA: W.H. Freeman.
- Langroudi, A., Jefferson, I., O'Hara-Dhand, K. & Smalley, I. (2014). Micromechanics of quartz sand breakage in a fractal context. *Geomorphology* **211**, 1–10.
- Mahmood, Z. & Iwashita, K. (2011). A simulation study of microstructure evolution inside the shear band in biaxial compression test. *Int. J. Numer. Analyt. Methods Geomech.* **35**, No. 6, 652–667.
- Mandelbrot, B., Passoja, D. & Paullay, A. (1984). Fractal character of fracture surfaces of metals. *Nature* **308**, No. 19, 721–722.
- Mathworks (2010). *MATLAB, version 7.0*. Natick, MA, USA: Mathworks, Inc..
- Mehring, J. & McBride, E. (2007). Origin of modern quartzarenite beach sands in a temperate climate, Florida and Alabama, USA. *Sedimentary Geol.* **201**, No. 3, 432–445.
- Mollon, G. & Zhao, J. (2012). Fourier–Voronoi-based generation of realistic samples for discrete modelling of granular materials. *Granular Matter* **14**, No. 5, 621–638.
- Mollon, G. & Zhao, J. (2013). Generating realistic 3D sand particles using Fourier descriptors. *Granular Matter* **15**, No. 1, 95–108.
- Mollon, G. & Zhao, J. (2014). 3D generation of realistic granular samples based on random fields theory and Fourier shape descriptors. *Comput. Methods Appl. Mech. Engng* **279**, 46–65.
- Mora, C. & Kwan, A. (2000). Sphericity, shape factor, and convexity measurement of coarse aggregate for concrete using digital image processing. *Cement Concrete Res.* **30**, No. 3, 351–358.
- Ollion, J., Cochenec, J., Loll, F., Escudé, C. & Boudier, T. (2013). TANGO: a generic tool for high-throughput 3D image analysis for studying nuclear organization. *Bioinformatics* **29**, No. 14, 1840–1841.
- Rousé, P., Fannin, R. & Shuttle, D. (2008). Influence of roundness on the void ratio and strength of uniform sand. *Géotechnique* **58**, No. 3, 227–231, <http://dx.doi.org/>.
- Santamarina, J. & Cho, G. (2004). Soil behaviour: the role of particle shape. In *Advances in geotechnical engineering: the Skempton conference* (eds R. Jardine, D. Potts and K. Higgins), vol. 1, pp. 604–617. London, UK: Thomas Telford.
- Soga, K. & Mitchell, J. (2005). *Fundamentals of soil behavior*, 3rd edn. New York, NY, USA: Wiley.
- Sukumaran, B. & Ashmawy, A. (2001). Quantitative characterisation of the geometry of discrete particles. *Géotechnique* **51**, No. 7, 619–627, <http://dx.doi.org/10.1680/geot.2001.51.7.619>.
- Tsomokos, A. & Georgiannou, V. (2010). Effect of grain shape and angularity on the undrained response of fine sands. *Can. Geotech. J.* **47**, No. 5, 539–551.
- Wadell, H. (1935). Volume, shape, and roundness of quartz particles. *J. Geol.* **43**, No. 3, 250–280.
- Wang, J. & Gutierrez, M. (2010). Discrete element simulations of direct shear specimen scale effects. *Géotechnique* **60**, No. 5, 395–409, <http://dx.doi.org/10.1680/geot.2010.60.5.395>.
- Yuan, C., Li, J., Yan, X. & Peng, Z. (2003). The use of the fractal description to characterize engineering surfaces and wear particles. *Wear* **255**, No. 1, 315–326.
- Zhao, B. & Wang, J. (2016). 3D quantitative shape analysis on form, roundness, and compactness with  $\mu$ CT. *Powder Technol.* **291**, 262–275.
- Zhao, B., Wang, J., Coop, M. R., Viggiani, G. & Jiang, M. (2015). An investigation of single sand particle fracture using X-ray micro-tomography. *Géotechnique* **65**, No. 8, 625–641, <http://dx.doi.org/10.1680/geot.4.P157>.
- Zheng, J. & Hryciw, R. (2015). Traditional soil particle sphericity, roundness and surface roughness by computational geometry. *Géotechnique* **65**, No. 6, 494–506, <http://dx.doi.org/10.1680/geot.14.P192>.
- Zhou, B. & Wang, J. (2015). Random generation of natural sand assembly using micro X-ray tomography and spherical harmonics. *Géotechnique Lett.* **5**, No. 1, 6–11, <http://dx.doi.org/10.1680/geolett.14.00082>.
- Zhou, B. & Wang, J. (2017). Generation of a realistic 3D sand assembly using X-ray micro-computed tomography and spherical harmonic-based principal component analysis. *Int. J. Numer. Analyt. Methods Geomech.* **41**, No. 1, 93–109.
- Zhou, B., Huang, R., Wang, H. & Wang, J. (2013). DEM investigation of particle anti-rotation effects on the micro-mechanical response of granular materials. *Granular Matter* **15**, No. 3, 315–326.
- Zhou, B., Wang, J. & Zhao, B. (2015). Micromorphology characterization and reconstruction of sand particles using micro X-ray tomography and spherical harmonics. *Engng Geol.* **184**, No. 14, 126–137.